Nanoscale

PAPER

View Article Online
View Journal | View Issue

Cite this: *Nanoscale*, 2023, **15**, 5705

$CsPbBr_3$ perovskite quantum dots grown within Fe-doped zeolite X with improved stability for sensitive NH_3 detection†

Wan Wu, Chunyu Zhao, Mingyou Hu, Aizhao Pan, * Wei Xiong and Yinghao Chen

Received 10th December 2022,
Accepted 15th February 2023

DOI: 10.1039/d2nr06923g

rsc.li/nanoscale

All-inorganic cesium lead halide ($CsPbX_3$, X = Cl, Br and I) perovskite quantum dots (QDs) have received enormous research interest because of their exceptional optoelectronic properties, but their low chemical stability under ambient conditions from inevitable defects restricts their practical applications. In an effort to enhance the stability of QDs, in this study, novel functional nanocomposites were fabricated by encapsulating perovskite QDs with zeolite X doped with iron ions. Focusing on the as-obtained nanocomposites labeled with QDs@Fe/X-*n*, doping a reasonable amount of Fe^{3+} ions can tremendously improve the order of perovskite lattices and reduce the halide vacancies. The results of stability improvement in nanocomposites with an optimal Fe^{3+} load (QDs@Fe/X-3) are presented. After storage in air for 100 days, the emission-peak position of the composites can remain almost unchanged, and the photoluminescence (PL) intensity can reach ~98% of the original intensity. Additionally, the PL intensity of QDs@Fe/X-3 can decrease immediately when exposing it to a NH_3 atmosphere at room temperature. The PL intensity can be linearly varied with a change in the NH_3 concentration. The original value of the PL can be rapidly recovered by separating the sample from the NH_3 environment. This work enables the QDs@Fe/X composite to be an ideal active material for ammonia sensing.

Introduction

All-inorganic cesium lead halide ($CsPbX_3$, X = Cl, Br and I) perovskite quantum dots (QDs) have attracted much attention in recent years due to their unique optoelectronic properties.[1–5] Their high photoluminescence quantum yields (PLQYs) (>90%), wide-range of colours, tunable bandgaps and narrow emission-bands make them excellent materials for next-generation optoelectronic devices. Up to now, the power conversion efficiency of perovskite solar cells (PSCs) has been improved to 25.7%,[6] owing to their wide light-absorption range, high carrier mobility and long electron–hole diffusion lengths.[7,8] Inspired by the achievements made in solar cells, cesium lead halide perovskites as the newcomers have been employed in the fields of light-emitting diodes, solar cells, anticounterfeit inks, and lasers.[9–12]

Owing to the increasing release of volatile ammonia from the chemical, pharmaceutical and agricultural industries, detection of ammonia has been extensively researched.[13,14] Various materials have been devoted to fabricating ammonia gas sensors, such as quantum dots, MOFs, and stimuli-responsive polymers, which have demonstrated excellent response.[15–17] However, the poor gas sensitivity and selectivity and low yields limit their practical applications. Recently, fluorescence perovskite-based sensors have achieved a superior response to NH_3 gas,[18–20] indicating fluorescence perovskite to be a potent material for fabricating highly sensitive gas sensors for ammonia. Generally speaking, a neat perovskite phase can easily bear the defect originating from some elements being removed from the crystal surface during annealing, such as Pb and X vacancy defects, reducing its performance and stability (vulnerable to various aging stresses such as oxygen, moisture and ultraviolet (UV) irradiation).[21–23] After surface encapsulation/modification or UV filtration, the lifetime of perovskite can be prolonged by a temporary separation.[24,25] Porous zeolite is an ideal candidate for encapsulating and stabilizing perovskite QDs due to its regularly arranged pores and channels.[26–28] Perovskite QDs embedded in zeolite can remain much more stable than the neat QDs under atmospheric moisture. Sun *et al.* reported a two-step synthesis of $CsPbX_3$ QDs embedded in zeolite Y.[29] The results showed that the stability of the QDs embedded in zeolite Y is improved compared to that of the neat QDs under ambient conditions. On this basis, Kim further found that zeolite X is a

Department of Chemistry, School of Chemistry, Xi'an Jiaotong University, Xianning West Road, 28, Xi'an 710049, China. E-mail: panaizhao2017032@xjtu.edu.cn

†Electronic supplementary information (ESI) available: Materials and characterization details, TEM and SEM elemental mapping profiles, and PL decay parameters. See DOI: https://doi.org/10.1039/d2nr06923g

better host, because it has a higher Al content in its framework (more extra framework cations may stabilize the QD guests).[30]

Moreover, doping metal ions is an effective strategy for reducing defects. A small number of di- or tri-valent metal cations can favour the nucleation of perovskite grains, the reduction of grain boundary defects, a decrease in trap-state density, an increase in the charge-carrier lifetime and an improvement of perovskite's properties.[31,32] For examples, Liu *et al.* revealed that Mn^{2+} can be easily inserted into the interstices of octahedral $[PbI_6]^{4-}$ to restrain the formation of vacancy defects to favour perovskite crystallization. Eventually, the efficiency of PSCs by excessively doping MnI_2 (1%) reaches 19.09%, which is superior to that of methylamine plumbum iodine ($MAPbI_3$)-based devices (17.68%).[31] Zhou *et al.* discovered that Eu^{3+}, Y^{3+} and Fe^{3+} have a positive impact on the power conversion efficiency (PCE) and device stability of PSCs.[32]

Inspired by metal ion doping and surface coating for improving the stability, we would like to propose multiple protection strategies that show that encapsulating perovskite within a metal ion-doped zeolite can effectively suppress the photo-induced regrowth and deterioration for an improvement of long-term storage stability of $CsPbBr_3$ perovskite QDs. In this work, we have introduced $CsPbBr_3$ QDs into iron-doped zeolite X (labelled with QDs@Fe/X) to achieve uniform QD dispersion, and tunable photoluminescence (PL) properties are induced *via* controlling the Fe dosage. The defect characteristics of QDs@Fe/X samples with different Fe contents were studied *via* time-resolved photoluminescence (TRPL) spectra and decay lifetime tests. Interestingly, the QDs@Fe/X nanocomposites can rapidly respond to ammonia gas with reversibility at room temperature. This finding is very encouraging for developing perovskite sensors using NH_3-responsive QDs@Fe/X matter in the future.

Experimental

Preparation of QDs@Fe/X

The synthesis of Fe/X with different Fe dosages, the preparation of QDs@Fe/X, and the study of NH_3 exposure are clarified as follows. A general route for preparing QDs@Fe/X composites is presented in Scheme 1, involving two separate processes, namely, crystallization under hydrothermal conditions for obtaining Fe-loaded zeolites X (Fe/X) and the *in situ* growth of $CsPbBr_3$ QDs inside Fe/X.

The Fe/X-*n* (n = 1, 2, 3 and 4) samples with different Fe dosages were synthesized by a molar ratio of $n(Al_2O_3) : n(SiO_2) : n(Na_2O) : n(H_2O) : n(Fe(NO_3)_3{\cdot}9H_2O) = 1 : 3.2 : 7.36 : 441.6 : x$ (x = 3.27×10^{-3}, 4.96×10^{-3}, 2.20×10^{-2} and 3.97×10^{-2}, respectively, and doping dosages of the metal were confirmed by adopting inductively coupled plasma (ICP) mass spectrometry). The mixture was vigorously stirred for 0.5 h for homogenization (800 rpm), followed by ageing for 8 h at room temperature. Finally, the solid was obtained by filtration and washed thoroughly several times with deionized water until the pH value reached 8–9, followed by drying at 105 °C and then milling.

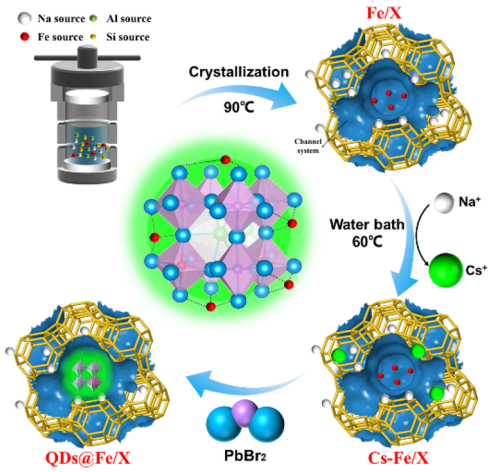

Scheme 1 Schematic illustration of preparation of QDs@Fe/X-*n* composites.

The QDs in Fe/X-*n* solution were prepared by the procedures reported by Sun[29] *et al.* First, Cs^+–Fe/X (Fe/X with Cs^+ *via* partial exchange) was prepared. Second, $PbBr_2$ solution was prepared. Finally, ODE (5.0 mL) and Cs^+–Fe/X (0.5 g) were blended, transferred into a three-neck flask (100 mL), and vacuum degassed for 30 min at 120 °C. Then, the temperature was increased to 150 °C under N_2 protection, followed by injection of the $PbBr_2$ solution. The mixture was stirred for 15 min and then cooled to room temperature. Ultimately, the product was washed (with *n*-hexane first followed by using isopropanol) and further centrifuged. The product was dried at 60 °C for 12 h. The resulting composites were labeled with QDs@Fe/X-*n* (n = 1, 2, 3 and 4 respectively). Various n values reflect different Fe dosages during preparation.

NH_3 exposure study

The experimental setup of the NH_3 exposure study was designed according to the previous studies.[20,33] NH_3 response experiments were performed in a sealed reaction tube (10 mL). A UV lamp (365 nm wavelength) was used as the optical excitation source to focus on samples. The various concentrations of NH_3 gases were obtained by diluting pure NH_3 gas with a certain amount of N_2 gas. Then the QDs@Fe/X-3 sample (0.02 g) was exposed to various concentrations (0–10 mL) of dry NH_3 gases with a syringe. The reaction tube had been evacuated in advance. Finally, the steady-state PL spectra were determined. During testing, dry NH_3 gas and air were injected alternately into the reaction tube with a syringe. The response, reversibility and stability of the samples were investigated in a "pure NH_3-air" cycle.

Results and discussion

Characterization of perovskite-bearing composites

The morphologies of the QDs@Fe/X-*n* samples are analysed here. Fig. 1a shows the SEM image of QDs@Fe/X-3. Many

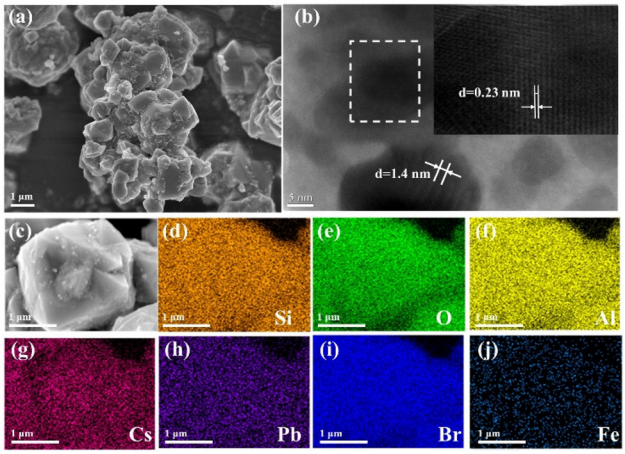

Fig. 1 SEM (a) and high-resolution TEM (b) images of QDs@Fe/X-3 and SEM image (c) along with elemental mapping profiles (d–j) of Si, O, Al, Cs, Pb, Br and Fe of the surveyed area of QDs@Fe/X-3.

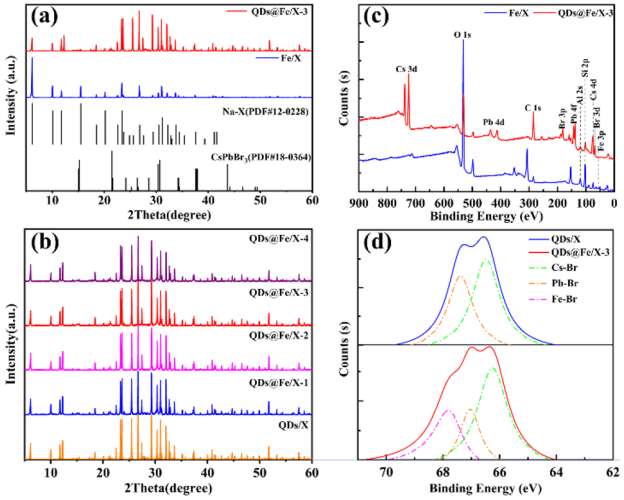

Fig. 2 PXRD patterns of Fe/X, QDs/X and QDs@Fe/X-*n* (a and b), XPS results of Fe/X and QDs@Fe/X-3 (c), and Br 3d XPS core-level spectra of QDs/X and QDs@Fe/X-3 (d).

cubic $CsPbBr_3$ QDs were evenly distributed at the Fe/X surface. The QDs@Fe/X-3 can have the most QDs distributed at the Fe/X surface with an increase in the Fe dosage (Fig. S1†). Fig. 1b shows a high-resolution TEM image of QDs@Fe/X-3. The gap between two adjacent fringes can reach 1.4 nm, corresponding to the distance between the two adjacent (1 1 1) lattice planes in faujasite (JCPDF #00-012-0228). Fringes with a gap of 0.23 nm can match (2 1 1) with the lattice planes in the $CsPbBr_3$ crystal.[34] All these results suggest that the $CsPbBr_3$ QDs were dispersed evenly on or within the zeolite crystal. Furthermore, by EDX, elemental mapping images can indicate uniform distributions of Si, O, Al, Cs, Pb, Br and Fe (Fig. 1d–j), confirming a successful growth of $CsPbBr_3$ QDs within Fe/X.

The crystal structures of QDs@Fe/X-*n* and Fe/X samples were determined by the PXRD method as shown in Fig. 2a and b. In Fig. 2a, compared with Fe/X (in blue), QDs@Fe/X-3 (in red) exhibits both the primary Fe/X diffraction peaks and an additional new peak (12.3°), originating from partial Cs^+ exchange into Fe/X (well matched with the reported Cs^+–Fe/X),[30,35,36] Moreover, the intensity of characteristic peak (6.1°) reduces significantly, which is clarified as follows. During Cs^+ exchange, the framework of Al might be slightly deprived due to a low hydrothermal stability of zeolite X, leading to damage to the framework structure of zeolite X and decreased crystallinity.[37] Besides, in Fig. S2,† a successful Cs^+ exchange can be verified based on a slight movement of all characteristic diffraction peaks to lower angles. A Cs^+ ion (a radius of 167 pm) has a larger covalent radius than a Na^+ ion (a radius of 102 pm), resulting in an increase in lattice spacing. These peak variations further confirm the formation of QDs within zeolite.

In Fig. 2b, XRD peaks from $CsPbBr_3$ (JCPDS #00-018-0364) QDs cannot be observed in QDs@Fe/X-*n*. The volume of crystal domains of the embedded QDs should be a few nm^3 at most, and thus the QDs diffraction signals are weaker than the micrometre-sized zeolite host. Furthermore, with an increase in the Fe dosage, the peaks from iron species cannot be detected in QDs/Fe@X-*n*, ascribed to a rather low iron content (highly scattered iron species).

Additionally, XPS technology (Fig. 2c) was utilized to verify the elemental composition of QDs@Fe/X-3 compared to that of Fe/X. Peaks of Fe/X from Al 2s, O 1s and Si 2p are observed ascribed to zeolite X.[38] Additional peaks of QDs@Fe/X-3 from Cs 3d, Pb 4f and Br 3d can confirm the presence of $CsPbBr_3$.[9,39,40] The iron content is too low to be detected. Besides, XPS core-level spectra (Fig. 2d) are shown for verifying the chemical states of Br 3d affected by Fe^{3+}.

Br^- in $CsPbBr_3$ QDs can be in two classes of chemical environments, namely, the higher band energy regions and the lower band energy regions (assigned to Pb–Br and Cs–Br complexes, respectively).[41,42] Compared to QDs/X, QDs@Fe/X-3 can have number-stable Cs–Br complexes, number-decreased Pb–Br species and number-increased Fe–Br species. A transformation from Pb–Br species to Fe–Br species is caused by the fact that a small number of trivalent iron ions can be easily embedded in the interstices of the perovskite *via* chemical bonding with Br^- ions to reduce bromine vacancy defects.[43] In total, after incorporating Fe^{3+} ions into $CsPbBr_3$ QDs, the number of Br^- ions can remarkably increase.

Optical properties of the as-fabricated perovskite-bearing composites

Optical properties of QDs/X and QDs@Fe/X-*n* nanocomposites with different Fe-dosages are given in Fig. 3a. With an increasing Fe dosage, the PL intensity of the samples increased first and then decreased (the strongest PL intensity in QDs@Fe/X-3). In Fig. 3b, compared to QDs/X, a blue shift of PL emission wavelengths was observed in all QDs@Fe/X-*n* samples (the largest blue shift was in QDs@Fe/X-3 – emission wavelength from 535.3 nm to 522.7 nm under 365 nm UV irradiation). This is ascribed to the *in situ* passivation and the quantum confinement effect of $CsPbBr_3$ QDs *via* Fe^{3+} and

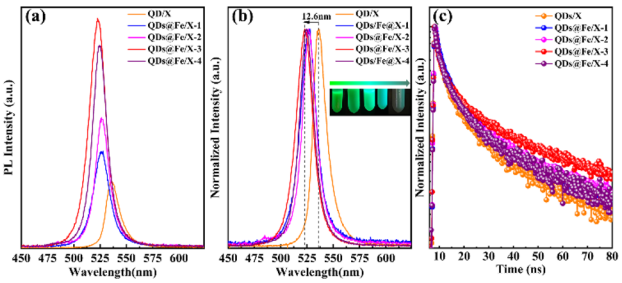

Fig. 3 PL spectra before (a) and after (b) normalization of QDs/X and QDs@Fe/X-*n* (insets in (b) are real photographs of the samples under 365 nm UV irradiation), and PL decay results (c) of QDs/X and QDs@Fe/X-*n*.

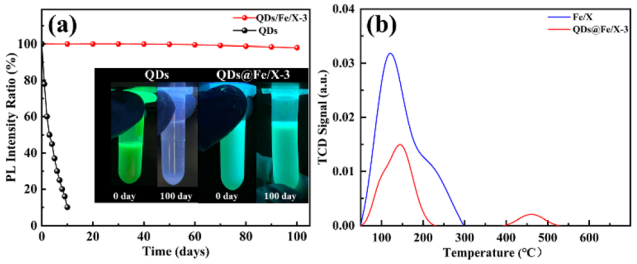

Fig. 4 Relative PLQYs (a) of QDs and QDs@Fe/X-3 under air exposure for 100 days (insets in (a) are real photographs of the samples under 365 nm irradiation), and NH_3-TPD curves of Fe/X and QDs@Fe/X-3 (b).

zeolite-X, respectively.[44,45] On the basis of Kubelka–Munk theory,[31,43] the higher the corresponding band gap energy level is and the shorter the emission wavelength is, the stronger the PL intensity is. Therefore, with an increasing Fe^{3+} dosage, the emission peak can show a slight blue shift (basically consistent with an increase in the PL intensity). Theoretically, the improved PLQY is associated with the improved short-range order and the reduced halide vacancies in lattices.[46] On the one hand, a small quantity of Fe^{3+} can aggregate near octahedral $[PbBr_6]^{4-}$ by chemical bonding with surrounding $[PbBr_6]^{4-}$, triggering the ordered arrangement and reducing the number of Pb^{2+} vacancies to improve the order of perovskite lattices.[47] On the other hand, Fe^{3+} can prevent ions from escaping and reduce bromine vacancy defects (Fig. 2d). Consequently, a small quantity of Fe^{3+} can favour an improvement in the stability of the perovskite structure. However, an overload of Fe^{3+} may cause the interstitial impurity defects to result in the decreased PLQY in QDs@Fe/X-4.

TRPL (Fig. 3c) tests were further conducted to study the defect effect of QDs/X and QDs@Fe/X-*n*. These decay data were fitted using a two-exponential decay model,[48] and the parameters are listed in Table S1.† There are two parts in PL decay curves (τ_1 and A_1 represent the decay time and percentage of intrinsic radiative recombination, respectively; τ_2 and A_2 represent the decay time and percentage of nonradiative recombination, respectively).[49,50] The two radiative times, namely, τ_1 and τ_2, may stem from structural defects of vacancies and surface states, respectively. τ_{avg} refers to the weighted-average PL decay time. The QDs@Fe/X-3 sample can have the maximum percentage of radiative recombination and the minimum percentage of nonradiative recombination (an average lifetime of 38.39 ns), which is much longer than other hybrid halide perovskites. This indicates that the QDs@Fe/X-3 specimen has a higher ratio of exciton recombination and less transition at defect states. Herein, self-passivation plays an important role in surface nonradiative recombination. The results suggest that Fe^{3+} doping with zeolite can suppress the defect recombination to extend the carrier lifetime of perovskites. Nonetheless, excess Fe^{3+} ions may increase the trap states and act as additional radiative relaxation channels, leading to the decrease in radiative decay rates and charge-carrier lifetime.[1,41,46,51,52] This agrees well with the conclusions drawn in Fig. 3a and b.

To study the environmental stability, the QDs@Fe/X-3 sample was exposed to ambient air for 100 days. In Fig. 4a, after 100 days of air exposure, the cyan brightness of QDs@Fe/X-3 is well maintained and the relative PLQY only drops by 2%, showing a high stability. By inference, this high stability may not be totally due to zeolite encapsulation. Thus, we measured the acidity of the samples (Fig. 4b). An obvious decrease in acid strength in zeolite X after the QD formation (2.941 mmol g^{-1} for Fe/X; 0.904 mmol g^{-1} for QDs@Fe/X-3) is verified, attributed to a partial deprivation of the framework of Al during the QD formation (resulting in the reduced acid densities). Furthermore, the Brunauer–Emmett–Teller (BET) results demonstrated the significant decrease in the surface area (891.0 to 166.1 m^2 g^{-1}) and pore volume (0.299 to 0.051 cm^3 g^{-1}) of Fe/X after QD growth, implying that the original zeolite framework structures were filled and collapsed after the formation of quantum dots (Table S2†). This is basically consistent with the XRD results.

Moreover, Fe/X itself is dominated by Lewis acid[37] and has no strong acid sites. However, QDs@Fe/X-3 has strong acid sites after introducing QDs with a decrease in Lewis acid and an increase in Brønsted acid. This may be caused by the fact that $CsPbBr_3$ QDs are confined in the interrupted nano-spaces of zeolite-X, where there are extensive dangling functional groups including Al–OH and Si–OH. Complex hydrogen bonds can be formed between the zeolite framework and perovskite halide anions.[44] This causes the electrons of silicon hydroxyl and aluminium hydroxyl groups to move into the cage (increasing the electron cloud density in the cage, making the hydroxyl group behave like a strong Brønsted acid). These strong interactions not only enhance the cohesion of the perovskite with zeolite-X, but also passivate imperfections and defects of the perovskite.

All results together demonstrate that embedding $CsPbBr_3$ QDs in Fe-doped zeolite X can obtain the ultra-stable perovskite/zeolite composite, thanks to encapsulation and *in situ* passivation.

Construction of a gas sensor using QDs@Fe/X

The superior long-term storage stability of QDs@Fe/X-3 in an air environment has prompted us to verify its applicability in an alkaline-gas sensor. The proof-of-concept experimental setup was designed (Fig. 5a). In detail, UV radiation (365 nm)

was used as the photoexcitation source to focus on a sample. Fluorescence emission spectra of the samples were recorded. QDs@Fe/X-3 was exposed to various concentrations of dry NH_3 gases using a syringe, and the response/recovery properties were recorded at room temperature. According to Fig. 5b, after exposure to NH_3, QDs@Fe/X-3 can emit strong blue-light under 365 nm UV radiation, and then it can be restored to the original state after NH_3 removal.

To confirm the change in luminescence properties by observation with the naked-eye, PL spectra of the composites in the presence of NH_3/air gases were achieved (Fig. 5c). After exposure to NH_3 gas, the cyan-emission peak at 522.7 nm can disappear (black line) and a broad emission band from 450 to 513 nm can be seen (red line). When air was introduced, the characteristic cyan emission peak reappeared (a small blue shift; gray line), and the PL intensity of the sample basically remained unchanged. This indicates a superior stability and reversibility of this perovskite sample. Later, we investigated the transient response of QDs@Fe/X-3 *via* an exposure to different concentrations of NH_3 gases (0–10 mL/10 mL), as shown in Fig. 5d. The PL intensity of QDs@Fe/X-3 quickly decreased with an increase in the NH_3 concentration. Fig. 5e reveals a linear response of the sample PL intensity with respect to the NH_3 concentration varying from 0 mL to 10 mL based on the following fitting equation: $Y = -71\,929X + 1\,231\,473$ ($R^2 = 0.954$). The aforementioned results can suggest that the QDs@Fe/X-3 composite has a fast response, good reversibility and high stability under NH_3 exposure, which enables the QDs@Fe/X-*n* materials to become promising candidates for the construction of state-of-the-art gas sensors.

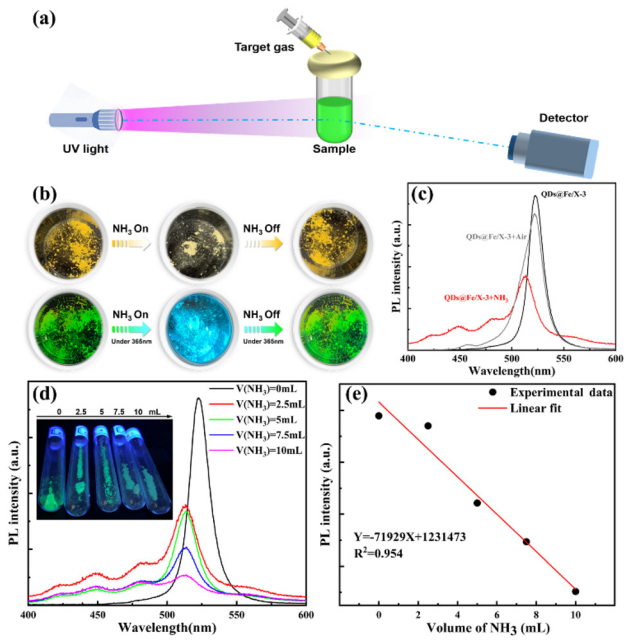

Fig. 5 Schematic of the experimental setup for NH_3 sensing (a); photographs of response–recovery cycles of the dynamic passivation of QDs@Fe/X-3 (b); PL emission spectra of pristine QDs@Fe/X-3 (black line), QDs@Fe/X-3 in the presence of NH_3 (QDs@Fe/X-3 + NH_3, red line), and QDs@Fe/X-3 under air exposure (QDs@Fe/X-3 + air, gray line) (c); PL spectra of QDs@Fe/X-3 exposed to various concentrations of NH_3 gases (d); linear relationship between response and NH_3 concentration (e).

Conclusions

We have successfully prepared QDs@Fe/X-*n* nanocomposites by *in situ* growth of $CsPbBr_3$ QDs embedded in iron ion-doped zeolite X. An efficient fluorescence quenching of $CsPbBr_3$ QDs, combined with time-resolved photoluminescence lifetime and stability test results, can confirm that embedding $CsPbBr_3$ QDs in Fe-doped zeolite X *via* encapsulation and *in situ* passivation is a workable strategy for the stabilization of QDs. Adopting an optimal Fe^{3+} dosage, after 100 days of storage in air, the position of the PL emission peak of the QDs@Fe/X-3 composite can be highly maintained, and the PL intensity can reach ~98% of the original value. Simultaneously, QDs@Fe/X-*n* composites can exhibit a fast response, good reversibility and high stability in the presence of NH_3 gas. We believe that the present work will enable practical applications of perovskite QDs/zeolite nanocomposite materials in gas sensors in the near future.

Author contributions

Wan Wu: investigation, visualization, and writing – original draft; Chunyu Zhao: investigation, visualization, and formal analysis; Mingyou Hu: conceptualization and writing – review & editing; Aizhao Pan: resources, conceptualization, and writing – review & editing; Wei Xiong: visualization and formal analysis; and Yinghao Chen: visualization and writing – review & editing.

Conflicts of interest

There are no conflicts to declare.

Acknowledgements

This work was primarily supported by the National Natural Science Foundation of China (NSFC Grants 21901196, 52172153, and 51802254). The authors also thank Gang Chang at the Instrument Analysis Center of Xi'an Jiaotong University for the assistance with the TEM and SEM analysis.

Notes and references

1 J. J. Yoo, G. Seo, M. R. Chua, T. G. Park, Y. Lu, F. Rotermund, Y. K. Kim, C. S. Moon, N. J. Jeon, J. P. Correa Baena, V. Bulović, S. S. Shin, M. G. Bawendi and J. Seo, *Nature*, 2021, **590**, 587–593.

2 J. Y. Kim, K. I. Shim, J. W. Han, J. Joo, N. H. Heo and K. Seff, *Adv. Mater.*, 2020, **32**, 2001868.

3 C. Zhao, H. Song, Y. Chen, W. Xiong, M. Hu, Y. Wu, Y. Zhang, L. He, Y. Liu and A. Pan, *ACS Energy Lett.*, 2022, **7**, 4389–4397.
4 D. Yang, M. Cao, Q. Zhong, P. Li, X. Zhang and Q. Zhang, *J. Mater. Chem. C*, 2019, **7**, 757–789.
5 J. Sun, A. Pan, K. Yan, P. Zhang, Y. Chen, W. Xiong, X. Chen and J. Hong, *Sens. Actuators, A*, 2022, **347**, 113948.
6 L. Li, Y. Wang, X. Wang, R. Lin, X. Luo, Z. Liu, K. Zhou, S. Xiong, Q. Bao, G. Chen, Y. Tian, Y. Deng, K. Xiao, J. Wu, M. I. Saidaminov, H. Lin, C. Q. Ma, Z. Zhao, Y. Wu, L. Zhang and H. Tan, *Nat. Energy*, 2022, **7**, 708–717.
7 A. Dey, J. Ye, A. De, E. Debroye, S. K. Ha, E. Bladt, A. S. Kshirsagar, Z. Wang, J. Yin, Y. Wang, L. N. Quan, F. Yan, M. Gao, X. Li, J. Shamsi, T. Debnath, M. Cao, M. A. Scheel, S. Kumar, J. A. Steele, M. Gerhard, L. Chouhan, K. Xu, X. g. Wu, Y. Li, Y. Zhang, A. Dutta, C. Han, I. Vincon, A. L. Rogach, A. Nag, A. Samanta, B. A. Korgel, C. J. Shih, D. R. Gamelin, D. H. Son, H. Zeng, H. Zhong, H. Sun, H. V. Demir, I. G. Scheblykin, I. Mora Seró, J. K. Stolarczyk, J. Z. Zhang, J. Feldmann, J. Hofkens, J. M. Luther, J. Pérez Prieto, L. Li, L. Manna, M. I. Bodnarchuk, M. V. Kovalenko, M. B. J. Roeffaers, N. Pradhan, O. F. Mohammed, O. M. Bakr, P. Yang, P. Müller Buschbaum, P. V. Kamat, Q. Bao, Q. Zhang, R. Krahne, R. E. Galian, S. D. Stranks, S. Bals, V. Biju, W. A. Tisdale, Y. Yan, R. L. Z. Hoye and L. Polavarapu, *ACS Nano*, 2021, **15**, 10775–10981.
8 M. Shekhirev, J. Goza, J. D. Teeter, A. Lipatov and A. Sinitskii, *J. Chem. Educ.*, 2017, **94**, 1150–1156.
9 A. Pan, J. Wang, M. J. Jurow, M. Jia, Y. Liu, Y. Wu, Y. Zhang, L. He and Y. Liu, *Chem. Mater.*, 2018, **30**, 2771–2780.
10 F. W. Liu, G. Biesold, M. Zhang, R. Lawless, J. P. Correa Baena, Y. L. Chueh and Z. Lin, *Mater. Today*, 2021, **43**, 185–197.
11 Y. H. Kim, S. Kim, A. Kakekhani, J. Park, J. Park, Y. H. Lee, H. Xu, S. Nagane, R. B. Wexler, D. H. Kim, S. H. Jo, L. Martínez Sarti, P. Tan, A. Sadhanala, G. S. Park, Y. W. Kim, B. Hu, H. J. Bolink, S. Yoo, R. H. Friend, A. M. Rappe and T. W. Lee, *Nat. Photonics*, 2021, **15**, 148–155.
12 B. Guo, R. Lai, S. Jiang, L. Zhou, Z. Ren, Y. Lian, P. Li, X. Cao, S. Xing, Y. Wang, W. Li, C. Zou, M. Chen, Z. Hong, C. Li, B. Zhao and D. Di, *Nat. Photonics*, 2022, **16**, 637–643.
13 P. Singh, C. S. Kushwaha, V. K. Singh, G. C. Dubey and S. K. Shukl, *Sens. Actuators, B*, 2021, **342**, 130042.
14 A. Fekete, A. K. Malik, A. Kumar and P. Schmitt-Kopplin, *Crit. Rev. Anal. Chem.*, 2010, **40**, 102–121.
15 M. S. Yao, J. W. Xiu, Q. Q. Huang, W. H. Li, W. W. Wu, A. Q. Wu, L. A. Cao, W. H. Deng, G. E. Wang and G. Xu, *Angew. Chem., Int. Ed.*, 2019, **58**, 14915–14919.
16 Y. Zhang, S. Yuan, G. Day, X. Wang, X. Yang and H. C. Zhou, *Coord. Chem. Rev.*, 2018, **354**, 28–45.
17 N. R. Tanguy, M. Thompson and N. Yan, *Sens. Actuators, B*, 2018, **257**, 1044–1064.
18 X. He, C. Yu, M. Yu, J. Lin, Q. Li, Y. Fang, Z. Liu, Y. Xue, Y. Huang and C. Tang, *Inorg. Chem.*, 2020, **59**, 1234–1241.
19 H. Huang, M. Hao, Y. Song, S. Dang, X. Liu and Q. Dong, *Small*, 2020, **16**, 1904462.
20 G. Li, C. She, Y. Zhang, H. Li, S. Liu, F. Yue, C. Jing, Y. Cheng and J. Chu, *Sens. Actuators, B*, 2021, **327**, 128918.
21 M. Saliba, T. Matsui, K. Domanski, J. Y. Seo, A. Ummadisingu, S. M. Zakeeruddin, J. P. Correa Baena, W. R. Tress, A. Abate, A. Hagfeldt and M. Grätzel, *Science*, 2016, **354**, 206–209.
22 J. M. Ball and A. Petrozza, *Nat. Energy*, 2016, **1**, 16149.
23 Z. Ni, H. Jiao, C. Fei, H. Gu, S. Xu, Z. Yu, G. Yang, Y. Deng, Q. Jiang, Y. Liu, Y. Yan and J. Huang, *Nat. Energy*, 2022, **7**, 65–73.
24 G. Grancini, C. Roldán Carmona, I. Zimmermann, E. Mosconi, X. Lee, D. Martineau, S. Narbey, F. Oswald, F. De Angelis, M. Graetzel and M. K. Nazeeruddin, *Nat. Commun.*, 2017, **8**, 15684.
25 X. Li, M. Ibrahim Dar, C. Yi, J. Luo, M. Tschumi, S. M. Zakeeruddin, M. K. Nazeeruddin, H. Han and M. Grätzel, *Nat. Chem.*, 2015, **7**, 703–711.
26 N. H. Heo, Y. Kim, J. J. Kim and K. Seff, *J. Phys. Chem. C*, 2016, **120**, 5277–5287.
27 B. Wang, Y. Yu, H. Zhang, Y. Xuan, G. Chen, W. Ma, J. Li and J. Yu, *Angew. Chem., Int. Ed.*, 2019, **58**, 18443–18448.
28 B. Wang, Y. Mu, H. Zhang, H. Shi, G. Chen, Y. Yu, Z. Yang, J. Li and J. Yu, *ACS Cent. Sci.*, 2019, **5**, 349–356.
29 J. Y. Sun, F. T. Rabouw, X. Yang, X. Y. Huang, X. P. Jing, S. Ye and Q. Y. Zhang, *Adv. Funct. Mater.*, 2017, **27**, 1704371.
30 J. Y. Kim, K. I. Shim, J. W. Han, J. Joo, N. H. Heo and K. Seff, *Adv. Mater.*, 2020, **32**, e2001868.
31 W. Liu, L. Chu, N. Liu, Y. Ma, R. Hu, Y. Weng, H. Li, J. Zhang, X. Li and W. Huang, *J. Mater. Chem. C*, 2019, **7**, 11943–11952.
32 L. Wang, H. Zhou, J. Hu, B. Huang, M. Sun, B. Dong, G. Zheng, Y. Huang, Y. Chen, L. Li, Z. Xu, N. Li, Z. Liu, Q. Chen, L. D. Sun and C. H. Yan, *Science*, 2019, **363**, 265–270.
33 Y. Hu, X. Ma, Y. Zhang, Y. Che and J. Zhao, *ACS Sens.*, 2016, **1**, 22–25.
34 Y. Jiang, J. F. Liao, Y. F. Xu, H. Y. Chen, X. D. Wang and D. B. Kuang, *J. Mater. Chem. A*, 2019, **7**, 13762–13769.
35 M. Omerašević, M. Lukić, M. Savić Biserčić, A. Savić, L. Matović, Z. Baščarević and D. Bučevac, *Nucl. Eng. Technol.*, 2020, **52**, 115–122.
36 A. Brundu and G. Cerri, *Microporous Mesoporous Mater.*, 2015, **208**, 44–49.
37 J. Xu, Z. Yang, Z. Li, H. Tang, B. Ren, R. Liu and T. Li, *Chin. J. Process Eng.*, 2018, **18**, 996–1002.
38 M. Zhang and X. Wang, *ACS Omega*, 2021, **6**, 18414–18425.
39 Z. J. Li, E. Hofman, J. Li, A. H. Davis, C. H. Tung, L. Z. Wu and W. Zheng, *Adv. Funct. Mater.*, 2018, **28**, 1704288.
40 X. He, V. Nguyen, Z. Jiang, D. Wang, Z. Zhu and W. N. Wang, *Catal. Sci. Technol.*, 2018, **8**, 2117–2123.
41 X. Li, Y. Wu, S. Zhang, B. Cai, Y. Gu, J. Song and H. Zeng, *Adv. Funct. Mater.*, 2016, **26**, 2435–2445.

42 J. Zhang, L. Zhang, P. Cai, X. Xue, M. Wang, J. Zhang and G. Tu, *Nano Energy*, 2019, **62**, 434–441.
43 W. Liu, N. Liu, S. Ji, H. Hua, Y. Ma, R. Hu, J. Zhang, L. Chu, X. Li and W. Huang, *Nano-Micro Lett.*, 2020, **12**, 119.
44 P. Wang, B. Wang, Y. Liu, L. Li, H. Zhao, Y. Chen, J. Li, S. Liu and K. Zhao, *Angew. Chem., Int. Ed.*, 2020, **59**, 23100–23106.
45 R. Cheng, E. Debroye, J. Hofkens and M. Roeffaers, *Catalysts*, 2020, **10**, 1352.
46 C. Bi, S. Wang, Q. Li, S. V. Kershaw, J. Tian and A. L. Rogach, *J. Phys. Chem. Lett.*, 2019, **10**, 943–952.
47 W. Zhao, Z. Yao, F. Yu, D. Yang and S. Liu, *Adv. Sci.*, 2018, **5**, 1700131.
48 V. Lesnyak, R. Brescia, G. C. Messina and L. Manna, *J. Am. Chem. Soc.*, 2015, **137**, 9315–9323.
49 Z. Liang, S. Zhao, Z. Xu, B. Qiao, P. Song, D. Gao and X. Xu, *ACS Appl. Mater. Interfaces*, 2016, **8**, 28824–28830.
50 S. Stranks, G. Eperon, G. Grancini, C. Menelaou, M. Alcocer, T. Leijtens, L. Herz, A. Petrozza and H. Snaith, *Science*, 2013, **342**, 341–344.
51 J. Lu, S. C. Chen and Q. Zheng, *Sci. China: Chem.*, 2019, **62**, 1044–1050.
52 M. Liu, H. Zhang, D. Gedamu, P. Fourmont, H. Rekola, A. Hiltunen, S. G. Cloutier, R. Nechache, A. Priimagi and P. Vivo, *Small*, 2019, **15**, 1900801.